# Optical CMOS-Based Method for Ionized Particle Identification and Extraction

Shou-long Xu,[1] Zhi-lin Wang,[1] Yu-bo Wang,[1] Shu-liang Zou,[1] Qing-xin Li,[1] and Yijun Zhong[1,*]

[1] *University of South China, Hengyang, Hunan 421001, China*

The integration of visible light imaging and ionizing radiation detection has long been hindered by their distinct physical mechanisms, posing challenges for advancements in nuclear safety monitoring and high-resolution imaging technologies. In this study, we propose a novel method for the discrimination and extraction of ionizing particles based on their spatial morphological features, leveraging a CMOS active pixel sensor (APS). By systematically analyzing the morphological characteristics of ionization response events from $\alpha$, $\beta$, and $\gamma$ radiation under varying gain and integration time conditions, parameters such as pixel count, aspect ratio, convexity, and compactness are extracted, with a focus on their relationship with the mean pixel value. The results demonstrate that $\alpha$-particle events exhibit significant differences in mean pixel value, pixel count, rectangularity, and convexity compared to $\beta$- and $\gamma$-particle events, while $\beta$- and $\gamma$-particle features show notable overlap, distinguishable primarily by mean pixel value. The proposed method effectively discriminates and extracts mixed radiation events, offering a foundation for future machine learning-based intelligent classification. This work highlights the potential of APS sensors in high-resolution optical imaging and nuclear radiation detection, providing critical insights for their applications in nuclear safety, emergency response, and facility decommissioning.

Keywords: ionizing particle detection, spatial morphological features, CMOS active pixel sensor, particle discrimination

## I. INTRODUCTION

Optical sensing technology and nuclear radiation detection are foundational in advancing high-resolution imaging and radiation monitoring [1–3]. Despite significant progress in both fields, their integration remains a challenge due to distinct physical mechanisms. CMOS sensors, with their high sensitivity, low noise, and high spatial resolution, have revolutionized optical imaging, enabling applications from single-photon detection to astronomical imaging [4, 5]. However, their potential in nuclear radiation detection remains underexplored. Additionally, CMOS technology demonstrates unique advantages in single-photon detection [6], and is applied in quantum imaging [7] and biological imaging, particularly showing high sensitivity and precision in quantum computing and medical imaging. By combining high spatial resolution with low noise characteristics, the application of CMOS sensors offers new perspectives for the development of nuclear radiation detection technology, helping to break down the barriers between optical sensors and nuclear radiation detection, thus promoting the integrated development of both fields [8, 9].

In recent years, CMOS sensor technology has made significant progress in optical sensing and high-resolution imaging, particularly in single-photon imaging and quantum imaging. CMOS technology has become one of the core technologies in this field due to its high spatial resolution and high temporal response characteristics. Single-photon imaging sensors are now widely used in quantum computing and biological imaging, with CMOS technology enabling high-sensitivity imaging under extremely low light conditions [10]. CMOS sensors also play an important role in high-resolution three-dimensional imaging. Combined with optical coherence tomography (OCT) technology, CMOS imaging has been practically applied in medical imaging and brain neuroscience [11, 12]. Additionally, CMOS technology has made breakthrough advancements in high-resolution astronomical imaging and miniature unmanned aerial vehicle (UAV) imaging systems, enabling more efficient imaging under complex atmospheric conditions or high-precision requirements [13].

Against this backdrop, researchers both domestically and internationally have gradually begun to explore the application of high-resolution pixel sensors in nuclear radiation detection. Currently, CMOS-based single-photon imaging sensors have demonstrated great potential in quantum imaging and spectral analysis [14–16]. For example, single-photon imaging sensors can be used to monitor radiation levels in the human body in real time, accurately pinpointing the location of radioactive sources using quantum imaging technology, with higher detection efficiency and lower dark count rates [17, 18]. In spectral analysis, single-photon imaging sensors can detect extremely weak light signals from biological entities, enabling high-resolution spectral measurements [19, 20]. Additionally, CMOS sensors in X-ray imaging can acquire high-quality images at low radiation doses, reducing radiation exposure to patients [21]. Meanwhile, in magnetic resonance imaging (MRI) applications, CMOS sensors can capture finer tissue structures, thereby improving image clarity and detail representation [22].

The widespread adoption of pixel sensors has driven the development of nuclear radiation detection. However, traditional energy-response methods for particle identification often suffer from low accuracy in complex radiation fields due to overlapping energy signatures [23–25]. In contrast, this study leverages CMOS imaging to analyze spatial morphological features of ionized particles, including parameters such as intensity, convexity, and compactness. By systematically investigating $\alpha$, $\beta$, and $\gamma$ particles, the proposed method overcomes the limitations of traditional techniques, offering a novel solution for high-precision particle identification. Domestically and internationally, related research still primarily focuses on detector structure design and the optimiza-

* Corresponding author.
E-mail address:zhongyijun152@126.com

tion of single parameters. Researchers have enhanced device performance through improvements in fabrication processes and testing circuits, such as improving the packaging technology of InGaAs single-photon detectors and optimizing the doping concentration and positioning of the P and N layers in CMOS-based single-photon avalanche diodes to improve photon detection efficiency [26, 27]. Meanwhile, improvements in the front-end electronics and geometric properties of CZT array detectors, as well as performance optimization of novel room-temperature semiconductor detector materials such as CdTe and TlBr, have further enhanced the sensitivity and resolution of the detectors [28, 29]. Although these studies have improved the detection capability of ionized particles to some extent, they have not yet addressed the spatial distribution characteristics of particle response events and intelligent particle identification methods. Traditional energy-response-based identification techniques mainly differentiate particle types by measuring pulse signals. However, in complex radiation fields, energy responses from different particles may overlap, leading to poor discrimination performance [30, 31]. In contrast, particle identification methods based on morphological features show significant advantages in improving identification accuracy and reducing misclassification rates, effectively addressing challenges in complex radiation fields.

This study introduces an innovative optical CMOS-based method for identifying and classifying ionized particles by analyzing their spatial morphological features. Through systematic analysis of $\alpha$, $\beta$, and $\gamma$ particle response events, we establish the feasibility of combining optical imaging and radiation detection to achieve reliable particle discrimination. This work highlights the potential for CMOS imaging in applications such as nuclear safety monitoring and high-resolution particle detection. A particle identification method based on ionized particle imaging morphological features is proposed. Simultaneously, event extraction is performed to provide training data support for subsequent machine learning-based intelligent particle classification. This study has significant potential in the field of environmental radiation monitoring, especially in radioactive contamination detection. By analyzing the interactions and spatial distribution characteristics of radiation particles, it provides new data support for assessing surface contamination levels [32]. In the field of biomedical imaging, this method can improve the accuracy of CT scans, more accurately capturing subtle changes in human tissues and diseased areas, thus aiding in early diagnosis and treatment of diseases [33]. Furthermore, in astronomical imaging, this method is expected to be applied in observations of distant celestial bodies. By capturing particle events from the depths of the universe, it provides new technological support for astronomical research [34].

## II. EXPERIMENT SETUP

Table 1 illustrates the experimental setup, where a SONY MT9P031 CMOS active pixel sensor was utilized. The sensor has a pixel size of 2.2 $\mu$m $\times$ 2.2 $\mu$m and an effective resolution of 2592 $\times$ 1944 pixels, supporting 8-10 bit digital signal output. The glass protective layer was removed to expose the silicon pixel array surface directly to radiation. Table 1 summarizes the key specifications of the sensor and radiation sources, providing a comprehensive overview of the experimental configuration.

Table 1. Experimental sample parameters

| Parameter | Value/Description |
|---|---|
| Sensor Pixel Size | $2.2\ \mu m \times 2.2\ \mu m$ |
| Sensor Resolution | 2592 $\times$ 1944 (horizontal $\times$ vertical) |
| $\alpha$ Source Activity | $2.9 \times 10^4$ Bq ($^{241}$Am) |
| $\beta$ Source Activity | $7.4 \times 10^7$ Bq ($^{63}$Ni) |
| $\gamma$ Source Activity | $9 \times 10^{14}$ Bq ($^{60}$Co) |

As illustrated in Figure 1, the experimental system was designed for the identification of ionized particles. The setup consists of two main regions: the irradiation chamber and the non-radioactive area. In the irradiation chamber, CMOS active pixel sensors (APS) are connected to the main board to form two sets of modules. One module corresponds to the $\alpha$ radioactive source ($^{241}$Am), while the other corresponds to the $\beta$ radioactive source ($^{63}$Ni). Both sources are housed inside a dark box to minimize ambient light interference during irradiation. A third $\gamma$ radioactive source ($^{60}$Co) is positioned externally, with the ability to raise or lower into the chamber.

Data acquisition is performed using a dual-system setup. The signals from the CMOS sensors are transmitted via data cables to PCs located in the non-radioactive area, ensuring operator safety. The fixed sample positions inside the dark box and the high-speed data transmission allow for stable and reliable measurements. This system enables simultaneous data collection from multiple radiation sources under controlled experimental conditions.

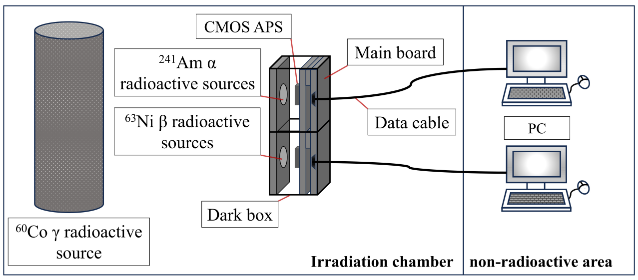


Fig. 1. Experimental system diagram

## III. DATA PROCESSING METHOD

The data processing pipeline combines pixel-level intensity analysis with morphological feature extraction to identify ionized particle events captured by the CMOS sensor. Key steps include:

(1) Pixel Intensity Calculation, the mean pixel value $M$ quantifies the overall brightness level of each response event:

$$M = \frac{1}{n \times m} \sum_{i=1}^{n} \sum_{j=1}^{m} I(i,j) \tag{1}$$

where $I(i,j)$ represents the pixel value at position $(i,j)$, while $n$ and $m$ denote the dimensions of the connected region.

(2) Morphological Feature Analysis: Region Area $P$, the number of pixels in a connected region:

Region Area $P$, the number of pixels in a connected region:

$$P = \sum_{i=1}^{n} \sum_{j=1}^{m} \delta(I(i,j)) \tag{2}$$

where $I(i,j)$ represents the pixel value of the pixel located in the $i$-th row and $j$-th column of the image, and $\delta$ is a selection function used to determine whether the pixel belongs to the connected region. $\delta(I(i,j))$ is a binary function defining connected regions with intensity thresholds $T$.

Rectangularity $R$, quantifies similarity to an ideal rectangle. When the region is circular, the rectangularity is approximately 0.785. Its calculation formula is as follows:

$$R = \frac{P}{P_{MER}} \tag{3}$$

with $P$ representing the area of the connected region, $P_{\mathrm{MER}}$ representing the minimum bounding rectangle's area.

Aspect Ratio ($V$), characterizes shape symmetry:

$$V = \frac{W}{H} \tag{4}$$

where $W$ and $H$ are the bounding rectangle's width and height, respectively.

Compactness ($O$), reflects shape uniformity:

$$O = \frac{S^2}{P} \tag{5}$$

where $S$ is the perimeter of the connected region.

Convexity ($H$), indicates edge complexity:

$$H = \frac{P}{F} \tag{6}$$

where $F$ is the convex hull's area.

These features are extracted for each event to provide a quantitative basis for identifying particle types. By leveraging CMOS sensors' high spatial resolution, the method ensures reliable event detection and classification in complex radiation fields.

## IV. RESULT

Figure 2 illustrates a typical $\alpha$-particle response event. As shown in the figure, the $\alpha$-particle response event appears as a bright spot on the image, where the pixel values of multiple pixels in the central region reach 255, and these pixels are closely connected, forming a high-intensity, uniform continuous region. This is because $\alpha$-particles have high energy and low penetration power. When interacting with the detector material, the high-density energy deposition causes the pixel values in the response region to rapidly reach saturation.

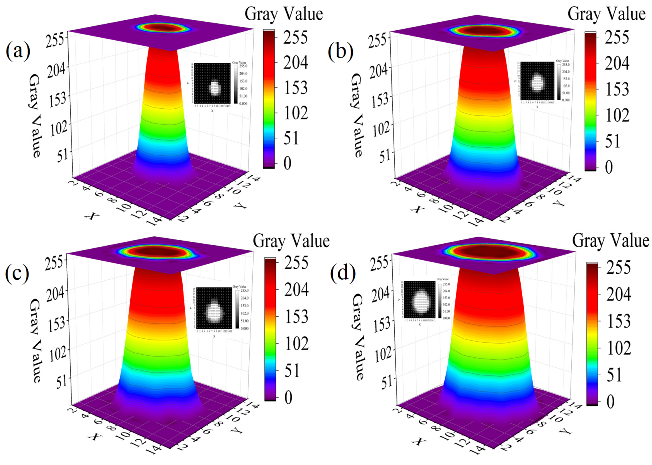


Fig. 2. $\alpha$-particle response event. (a) $\alpha$-particle response event under 9 dB conditions. (b) $\alpha$-particle response event under 16 dB conditions. (c) $\alpha$-particle response event under 32 dB conditions. (d) $\alpha$-particle response event under 63 dB conditions.

Figure 3 illustrates a typical $\beta$-particle response event. As seen in the figure, the $\beta$-particle response event is noticeably weaker than the $\alpha$-particle response, and the response area is smaller. Under low gain conditions, only the pixel value of one pixel in the response signal exceeds 200; however, when the gain reaches 32 dB or higher, the pixel values of multiple pixels reach higher levels. This is because $\beta$-particles have a smaller mass and stronger penetration ability, resulting in a much lower ionization rate compared to $\alpha$-particles of the same energy. When interacting with the detector material, significant scattering occurs, causing the energy of the $\beta$-particle to gradually attenuate along its path, resulting in a lower event intensity and energy concentrated in a localized region.

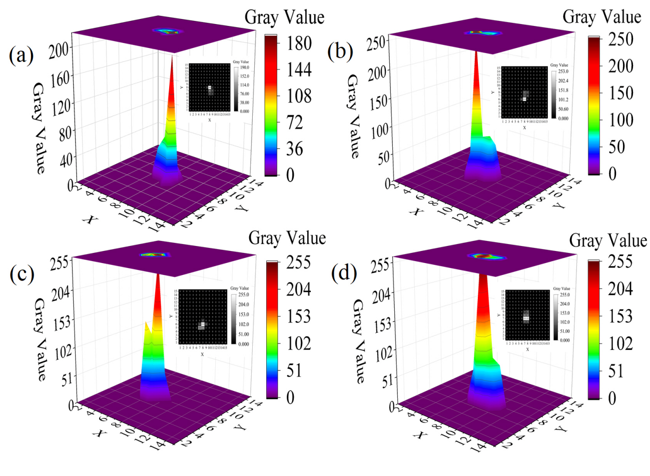


Fig. 3. $\beta$-particle response event. (a) $\beta$-particle response event under 9 dB conditions. (b) $\beta$-particle response event under 16 dB conditions. (c) $\beta$-particle response event under 32 dB conditions. (d) $\beta$-particle response event under 63 dB conditions.

Figure 4 illustrates a typical $\gamma$-particle response event. As seen in the figure, the $\gamma$-particle response is weaker than the $\beta$-particle response, but its shape is similar to that of the $\beta$-event. When the gain is 9 dB, only one pixel in the response event has a value exceeding 140; when the gain is 32 dB, the pixel value of a single pixel reaches 255. This is because $\gamma$-particles do not have direct ionization capability and, compared to $\beta$-particles, they have stronger penetration ability. When interacting with the detector material, $\gamma$-particles primarily produce secondary electrons through the photoelectric effect, Compton scattering, and pair production, which then generate response events in the detector. Since $\beta$-particles are essentially high-speed electron streams, $\gamma$-particles ultimately produce response events similar to those of $\beta$-particles through ionization effects induced by electrons in the detector.

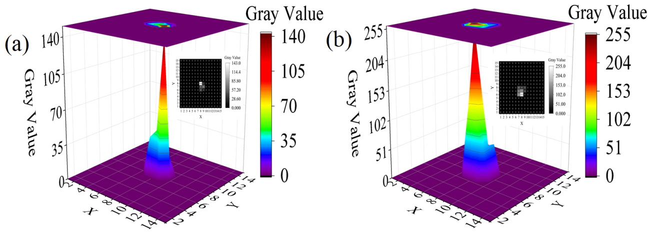


Fig. 4. $\gamma$-particle response events under different gain conditions. (a) $\gamma$-particle response event under 9 dB conditions. (b) $\gamma$-particle response event under 32 dB conditions.

In summary, the experimental results indicate that as the gain increases, the pixel values of the response events for $\alpha$, $\beta$, and $\gamma$ particles significantly increase, with $\alpha$ particle events showing the most pronounced changes. This provides a basis for effectively identifying $\alpha$ particles in mixed radiation fields. At the same time, changes in their morphology can also be observed, making quantitative analysis necessary. The specific changes are studied by calculating the mean pixel value, the number of pixels involved in response events, rectangularity, aspect ratio, compactness, and convexity.

Figure 5 illustrates the relationship between gain, integration time, and the mean pixel value distribution of response events.As shown in the figure, with an increase in gain, the mean pixel value of various events shows an upward trend, manifested as a rightward shift in the curve's peak. For $\alpha$ responses, when the gain is 9 dB, events are mainly distributed between a mean pixel value of 80 to 115, with the peak around 100. Under a gain of 63 dB, the peak shifts closer to 115, with events concentrated between 105 and 125. At this point, the peak becomes higher, and the peak width narrows.

In contrast, the mean pixel value curve for $\beta$ events changes more gradually. At a gain of 9 dB, events are primarily concentrated between a mean pixel value of 15 to 30, with a distinct peak at 20. At a gain of 63 dB, the peak approaches 100, with events distributed between 50 and 130. In this case, the peak height decreases, and the peak width expands significantly.The curve distribution for $\gamma$ events is similar to that of $\beta$ events. At a gain of 9 dB, events are mainly concentrated around a mean pixel value of 14, with a distinct peak at 14. When the gain increases to 32 dB, the peak shifts to around 17, with the peak width also expanding and the peak height decreasing.The experimental results show that increasing the gain significantly enhances the pixel values in the response events and gradually leads them to a saturated state, with the effects being more pronounced for $\beta$ and $\gamma$ events. This is because the gain increase causes an exponential growth in event intensity. The strong ionization capability of $\alpha$ particles makes their events more distinct, resulting in a more concentrated distribution under high gain. For $\beta$ and $\gamma$ particles, their low energy deposition means that an increase in gain amplifies and enhances originally weaker events. Additionally, the scattering effects and interactions between particles lead to a broader distribution. In contrast, the integration time mainly affects the cumulative amount during event sampling and has a relatively smaller impact on the mean pixel value distribution.

Figure 6 illustrates the distribution range of mean pixel values for response events under different gain conditions. The main distribution range of the curves was effectively determined using the half-maximum method to define the core distribution area of event morphological characteristics. As shown in the figure, when the gain is 9 dB, the mean pixel values for $\alpha$ events are primarily distributed between 57 and 71, $\beta$ events between 15 and 32, and $\gamma$ events between 12 and 18. When the gain reaches 32 dB, the range for $\alpha$ events shifts to 105–122, $\beta$ events to 31–78, and $\gamma$ events to 15–24. As the gain increases, the main distribution range for $\alpha$ events becomes narrower, while the ranges for $\beta$ and $\gamma$ events become wider.

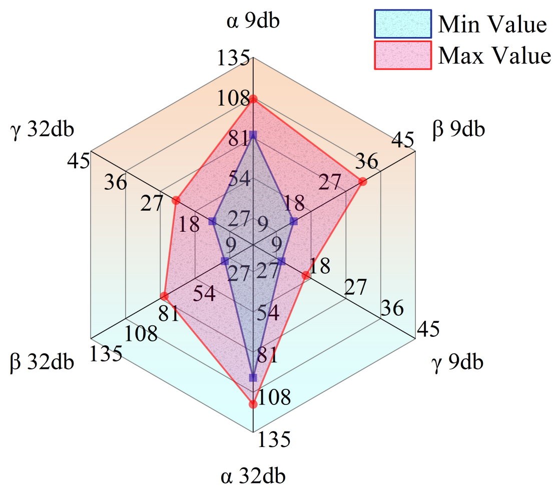


Fig. 6. Main range of mean pixel values for response events.

Figure 7 shows the relationship between gain, integration time, and counts of pixels in events. From Figure 7(a), it can be observed that the counts of pixels in $\alpha$ events increase significantly with the gain. Under 9 dB conditions, the counts of pixels are distributed between 50 and 75, with a clear peak near 60. When the gain reaches 63 dB, the counts of pixels rise to between 115 and 140, with the peak appearing near 130. At this point, the peak becomes lower, and the width of the distribution broadens. In contrast, the pixel count dis-

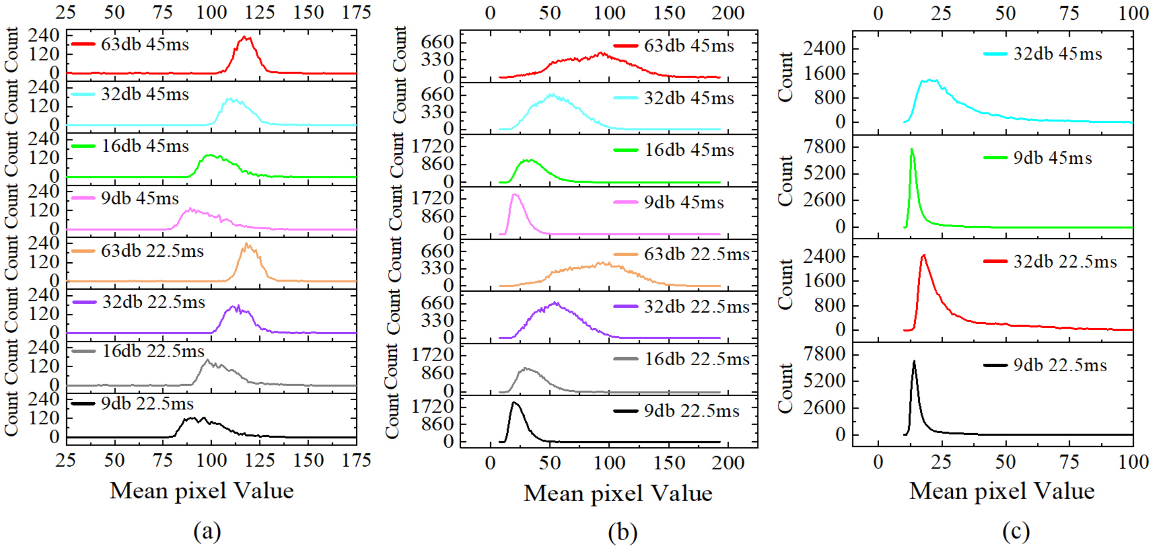


Fig. 5. Mean pixel value of response events. (a) Mean pixel value of response events for $\alpha$ particles. (b) Mean pixel value of response events for $\beta$ particles. (c) Mean pixel value of response events for $\gamma$ particles.

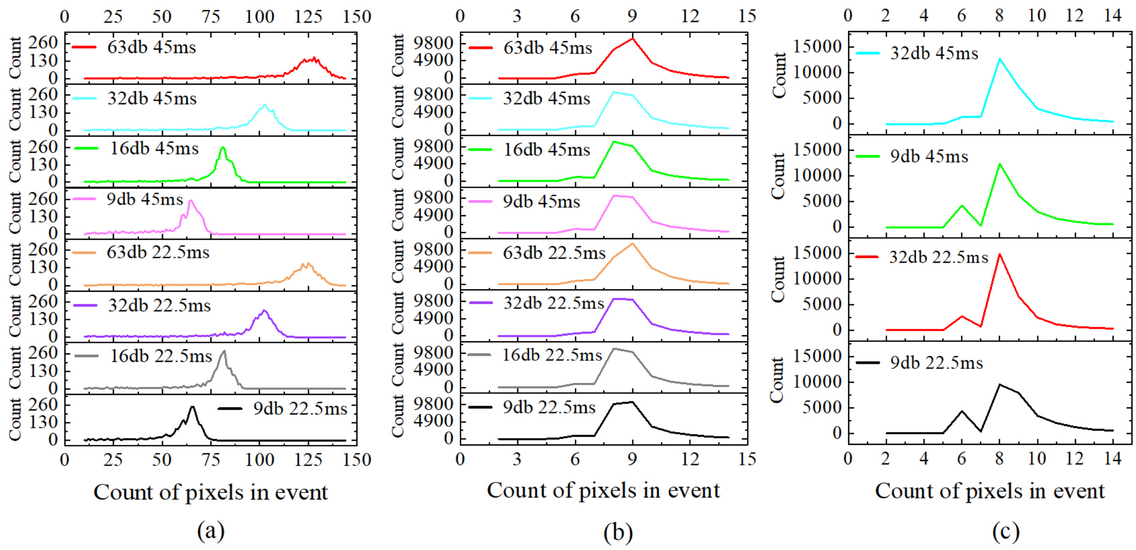


Fig. 7. Counts of pixels in events. (a) Counts of pixels in $\alpha$-particle response events. (b) Counts of pixels in $\beta$-particle response events. (c) Counts of pixels in $\gamma$-particle response events.

tribution curves for $\beta$ and $\gamma$ events remain relatively stable under different gain conditions. From Figure 7(b), it can be seen that under low gain conditions, the counts of pixels in $\beta$ events are primarily concentrated between 8 and 9. When the gain reaches 63 dB, a distinct peak appears at 9. The pixel count distribution trend for $\gamma$ events is similar to that of $\beta$ events, as shown in Figure 7(c), where the peak counts of pixels consistently appear at 8 under all gain conditions. This indicates that the increase in gain significantly affects the counts of pixels in $\alpha$ events, while having relatively little impact on $\beta$ and $\gamma$ events. This is because $\alpha$ radiation has strong ionization capability, and the pixel values of weakly affected surrounding pixels in response events are amplified under high gain conditions. For $\beta$ and $\gamma$ radiation, the ionization capability is relatively weaker, and fewer surrounding pixels are affected, resulting in limited enhancement of the events with increasing gain. Similarly, integration time does not significantly affect the counts of pixels in the events.

Figure 8 shows the relationship between gain, integration time, and the convexity distribution of response events. From Figure 8(a), it can be observed that the convexity of $\alpha$ events shows a slow upward trend with increasing gain, while its peak value and peak width remain relatively stable. Under 9 dB conditions, the convexity of events is primarily concentrated between 0.85 and 0.87, with a distinct peak at 0.86. At 63 dB, the convexity range expands to 0.89–0.91, with a peak at 0.9.Compared to $\alpha$ events, the convexity distribution of $\beta$ and $\gamma$ events remains stable within a relatively fixed range under different gain conditions. Observing Figures 8(b) and 8(c), the convexity of $\beta$ events is concentrated between

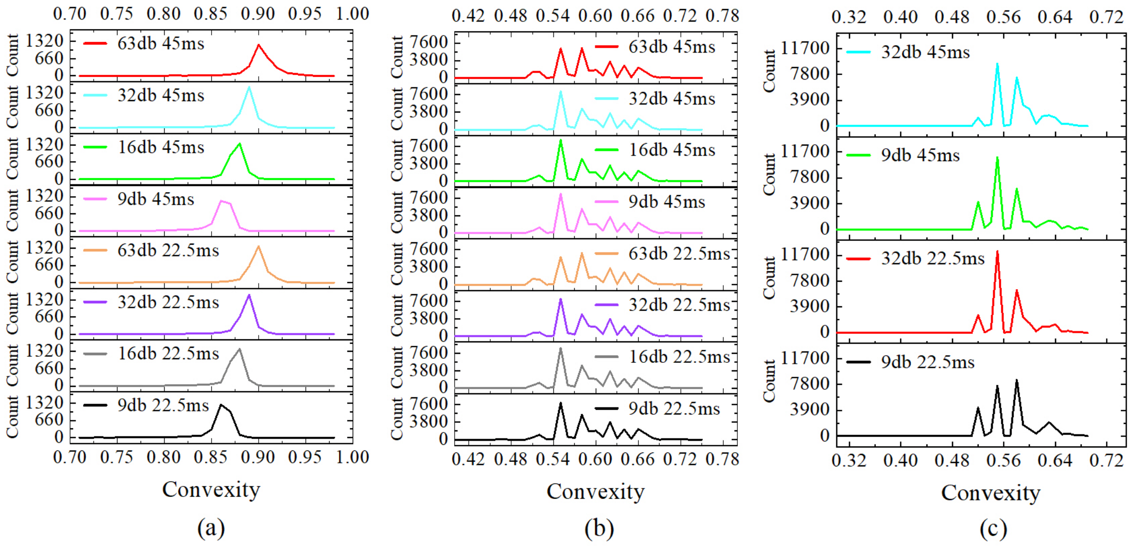


Fig. 8. Convexity of response events. (a) Convexity of $\alpha$-particle response events. (b) Convexity of $\beta$-particle response events. (c) Convexity of $\gamma$-particle response events.

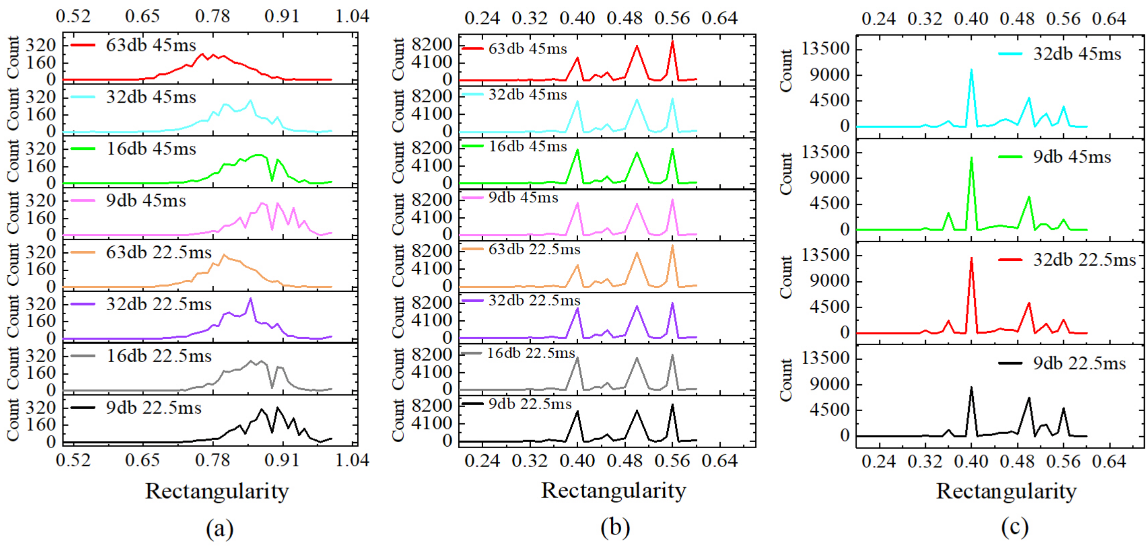


Fig. 9. Rectangularity of response events. (a) Rectangularity of $\alpha$-particle response events. (b) Rectangularity of $\beta$-particle response events. (c) Rectangularity of $\gamma$-particle response events.

0.55 and 0.66, with significant peaks at 0.55 and 0.58. When the gain reaches 63 dB, the peak at 0.55 decreases, while the peak at 0.58 increases relatively. The convexity of $\gamma$ events is lower compared to $\beta$ events, primarily distributed between 0.52 and 0.56, with the peak at 0.5 significantly increasing at 32B. This indicates that increasing the gain generally leads to a rise in the convexity of the three types of events, resulting in more regular event morphology, with the most significant changes observed in $\alpha$ events. This is because $\alpha$ particles have stronger ionization capabilities compared to $\beta$ and $\gamma$ particles, making the effect of increased gain more pronounced. The changes in the convexity of $\beta$ and $\gamma$ events require higher gain levels to become evident. Integration time does not have a significant impact on the convexity of the events.

Figure 9 shows the relationship between gain, integration time, and the rectangularity distribution of response events. As shown in the figure, with increasing gain, the rectangularity of $\alpha$ events shows a downward trend. Under 9 dB and 16 dB conditions, the rectangularity of events is mainly concentrated between 0.77 and 0.98, with multiple peaks near 0.89. At 63 dB, the rectangularity range narrows to 0.70–0.91, with the peak appearing near 0.8. Although the peak value decreases compared to 32 dB, the peak width does not change significantly. For a standard circle, the rectangularity is approximately 0.785, indicating that increasing the gain causes the morphology of $\alpha$ events in dark images to become closer to circular. This may be because higher gain enhances the sensor's efficiency in characterizing particles, making the response to ionizing radiation more sensitive and reducing shape distortion caused by ionizing particle tracks or internal

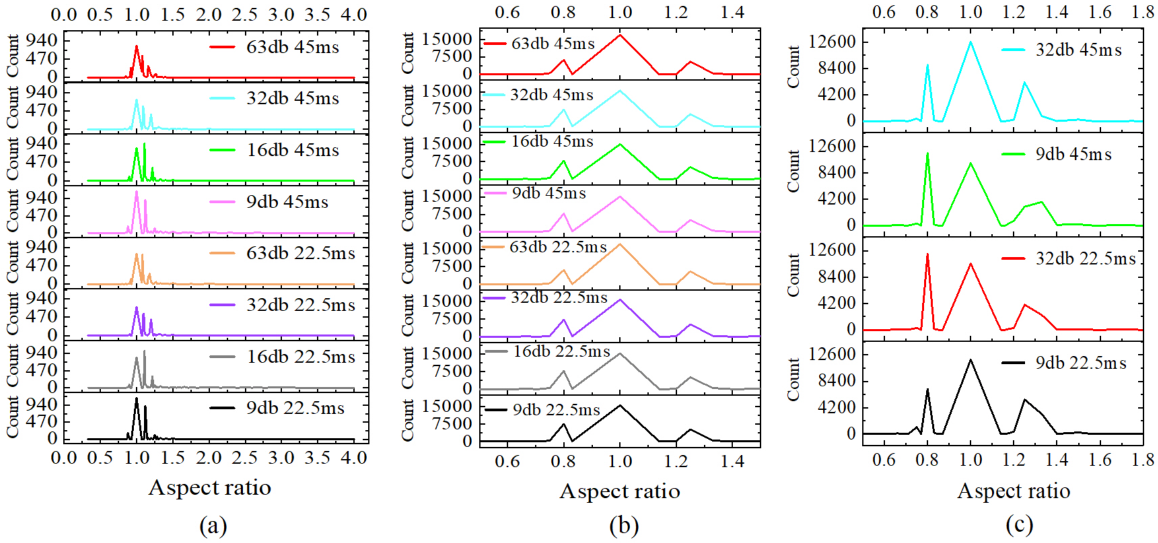


Fig. 10. Aspect ratio of response events. (a) Aspect ratio of $\alpha$-particle response events. (b) Aspect ratio of $\beta$-particle response events. (c) Aspect ratio of $\gamma$-particle response events.

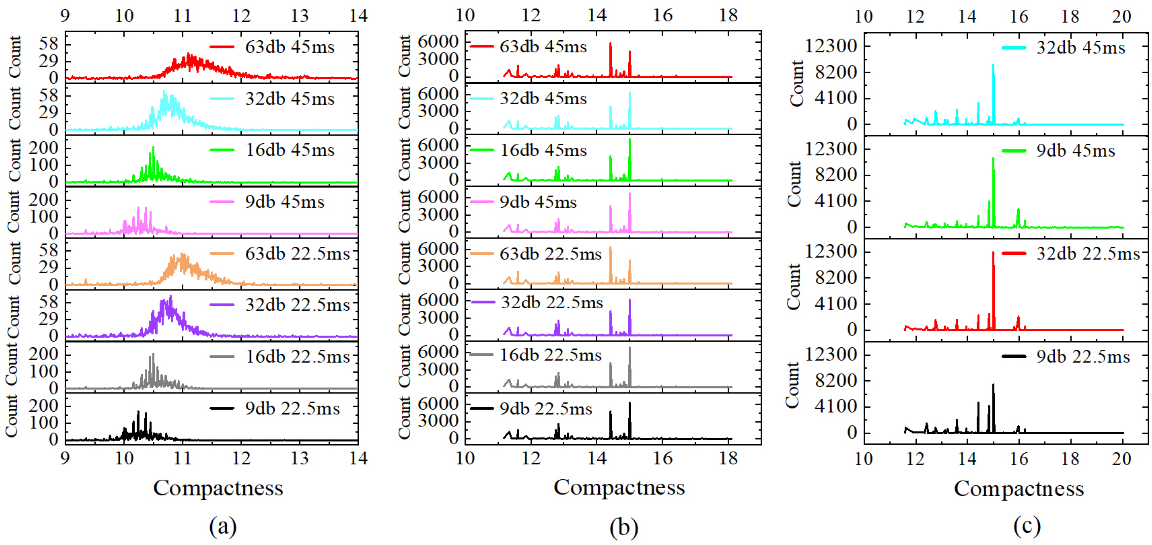


Fig. 11. Compactness of response events. (a) Compactness of $\alpha$-particle response events. (b) Compactness of $\beta$-particle response events. (c) Compactness of $\gamma$-particle response events.

pixel structure non-uniformities. In contrast, the rectangularity distribution of $\beta$ and $\gamma$ events remains relatively stable with changes in gain. The rectangularity of both is concentrated between 0.4 and 0.56 under different gain conditions, with distinct peaks at 0.4, 0.5, and 0.56. Some $\gamma$ events exhibit lower rectangularity than $\beta$ events. This indicates the presence of depressions or irregularities in the morphology of these two types of events. This may result from the complexity of particle interactions, scattering effects, and the high-resolution pixel structure of the sensor. Integration time does not significantly affect the changes in the rectangularity of events.

Figure 10 shows the relationship between gain, integration time, and the aspect ratio distribution of response events. From Figure 10(a), it can be observed that as the gain increases, the aspect ratio distribution of $\alpha$ events becomes more compact, with the peak concentrated near 1. A distinct peak forms at 1, and as the gain increases, the peak shifts closer to 1, showing a more pronounced centralization trend. This indicates that $\alpha$ events tend to exhibit a more symmetric or circular morphology under high gain, consistent with the results observed in the changes in rectangularity and convexity. In contrast, the aspect ratio distributions of $\beta$ and $\gamma$ events remain relatively stable and show some similarity as the gain increases. From Figures 10(b) and 10(c), the aspect ratios of $\beta$ and $\gamma$ events are mainly distributed between 0.8 and 1.25, with a distinct peak at 1. Additionally, $\gamma$ events show some distribution at 1.33. This indicates that although irregularities exist in the morphology of both event types, their overall geometric characteristics exhibit a degree of symmetry or unifor-

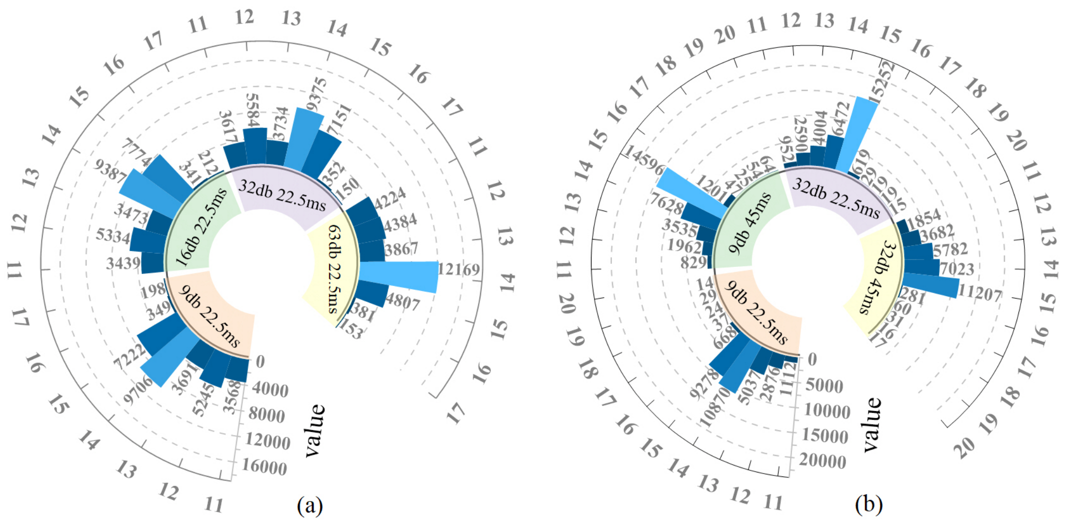


Fig. 12. Rounded Compactness of response events. (a) Compactness of $\beta$-particle response events. (b) Compactness of $\gamma$-particle response events.

mity. This may be due to the scattering of particles within the detector, leading to irregularities in event morphology, but these irregularities are not significant enough to affect the overall aspect ratio distribution. Similarly, integration time does not significantly affect the changes in the aspect ratio of events.

Figure 11 illustrates the relationship between gain, integration time control, and the distribution of event compactness. As shown in Figure 11(a), the compactness of $\alpha$-events increases with the enhancement of gain. Under the 9 dB condition, the compactness mainly ranges from 10 to 11; however, under the 63 dB condition, the range expands to 10.5 to 11.5, with a distinct peak near 11. This change further confirms that $\alpha$-events tend to adopt a symmetrical or circular shape at high gain. In contrast, the compactness distribution of $\beta$- and $\gamma$-events is more dispersed. As observed in Figures 11(b) and 11(c), both exhibit compactness primarily between 12 and 15, with several local peaks within this range. Additionally, some $\gamma$-events display a compactness greater than 16.

Figure 12 illustrates the relationship between gain, integration time control, and the rounded-down compactness of $\beta$ and $\gamma$ events. From the figure, it can be more clearly observed that under high gain conditions, there are differentiated characteristics in the compactness of $\beta$ and $\gamma$ rays. The compactness of $\beta$ events is concentrated between 14 and 15, while the compactness of $\gamma$ events is concentrated between 15 and 16. This phenomenon indicates that $\gamma$-events are more flattened compared to $\beta$-events. This could be due to the higher penetrating power of $\gamma$ particles, which induce scattering effects in the detector, making the propagation path more complex and resulting in a flatter shape.

Using a circle and a square as the reference, the shape characteristics corresponding to different ranges of compactness are defined, and the compactness $C$ is mapped to the interval $[0,1]$ using the following normalization formula:

$$C_{\text{normalized}} = \frac{C - C_{\min}}{C_{\max} - C_{\min}} \tag{7}$$

Here, $C_{\min}$ is the minimum compactness value in the data, $C_{\max}$ is the maximum compactness value in the data, and $C$ is the compactness value to be normalized. The selection of $C_{\min}$ and $C_{\max}$ is based on the statistical values of the compactness for $\alpha$, $\beta$, and $\gamma$ events, with final values determined to be 10 and 20, respectively. According to the formula, the compactness of a circle is $4\pi$, resulting in a normalized value of 0.256, while the compactness of a square is 16, yielding a normalized value of 0.6.

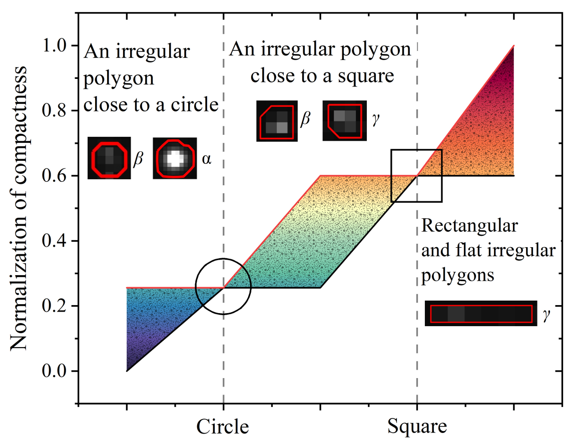


Fig. 13. Normalized compactness feature map for $\alpha$, $\beta$, and $\gamma$ events.

Figure 13 shows the normalized compactness feature map for $\alpha$, $\beta$, and $\gamma$ events. From the figure, it can be observed that for $\alpha$-events and some $\beta$-events, their shapes are irregular polygons close to a circle, with normalized values less than 0.256. For some $\beta$- and $\gamma$-events, their shapes are irregular polygons close to a square, with normalized values between 0.256 and 0.6. For some $\gamma$-events, their shapes are rectangular or flattened polygons, with normalized values greater than 0.6. By integrating the analysis of compactness, rectangularity, convexity, and aspect ratio, we can achieve a more

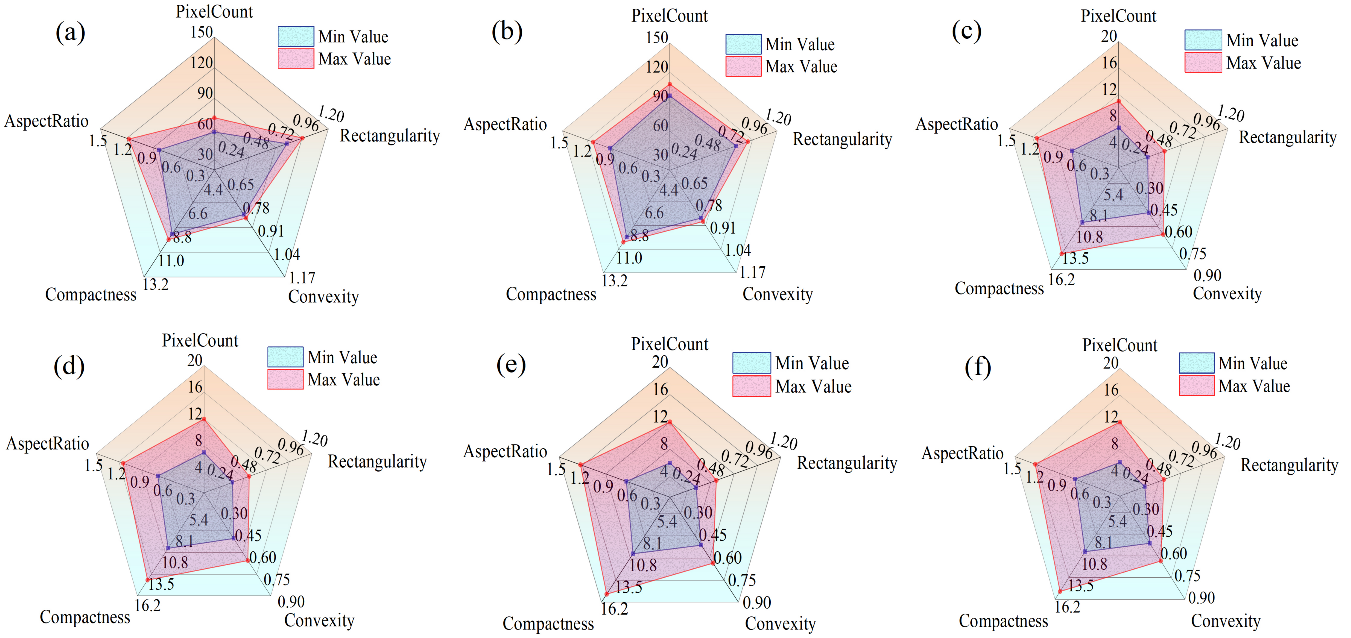


Fig. 14. Main range description of five features for different types of events under various conditions. (a) Main range of the five features for $\alpha$ events under 9 dB condition. (b) Main range of the five features for $\alpha$ events under 32 dB condition. (c) Main range of the five features for $\beta$ events under 9 dB condition. (d) Main range of the five features for $\beta$ events under 32 dB condition. (e) Main range of the five features for $\gamma$ events under 9 dB condition. (f) Main range of the five features for $\gamma$ events under 32 dB condition.

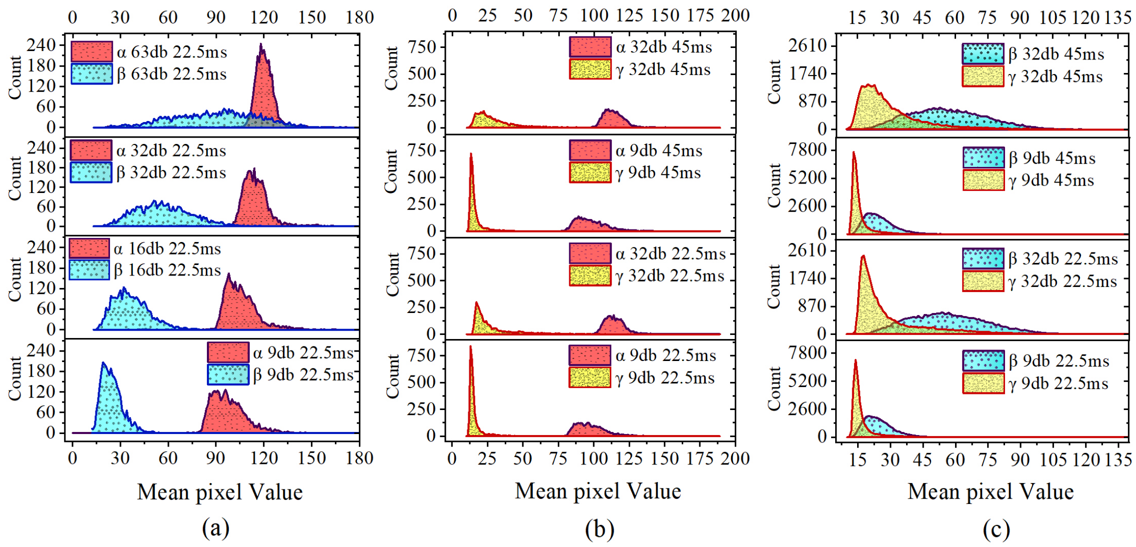


Fig. 15. Comparison of mean pixel values for response events. (a) Mean pixel values for $\alpha$ and $\beta$ response events. (b) Mean pixel values for $\alpha$ and $\gamma$ response events. (c) Mean pixel values for $\beta$ and $\gamma$ response events.

accurate understanding of the morphological characteristics of the response events.

Figure 14 shows how the main distribution ranges of the morphological features of response events change with gain. From Figures 14(a) and 14(b), it can be seen that at a gain of 9 dB, the pixel count of $\alpha$-events is mainly distributed between 57 and 71, whereas at 32 dB, the distribution range expands to 96 to 108, with a span of 12. The variation in rectangularity is relatively smooth, with its maximum value decreasing from 0.95 to 0.9 and its minimum value dropping from 0.8 to 0.78, leading to a smaller span. The distribution range of convexity mainly stays between 0.85 and 0.91, while the compactness is primarily concentrated between 10.5 and 11.3, with a relatively stable range span. The aspect ratio slightly decreases with the increase in gain, remaining between 0.88 and 1.3.

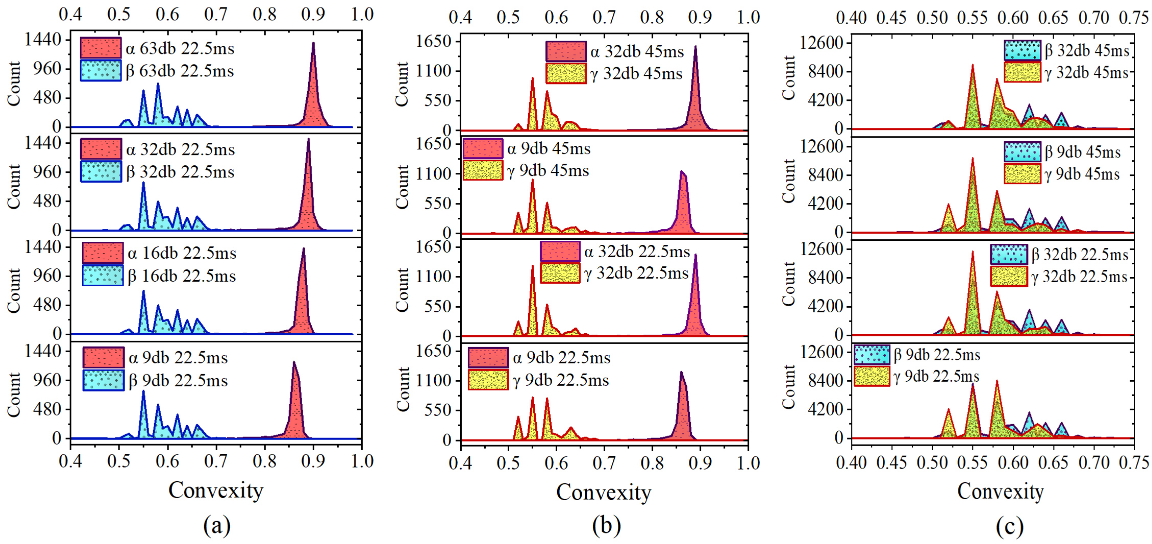


Fig. 16. Comparison of convexity for response events. (a) Convexity of $\alpha$ and $\beta$ response events. (b) Convexity of $\alpha$ and $\gamma$ response events. (c) Convexity of $\beta$ and $\gamma$ response events.

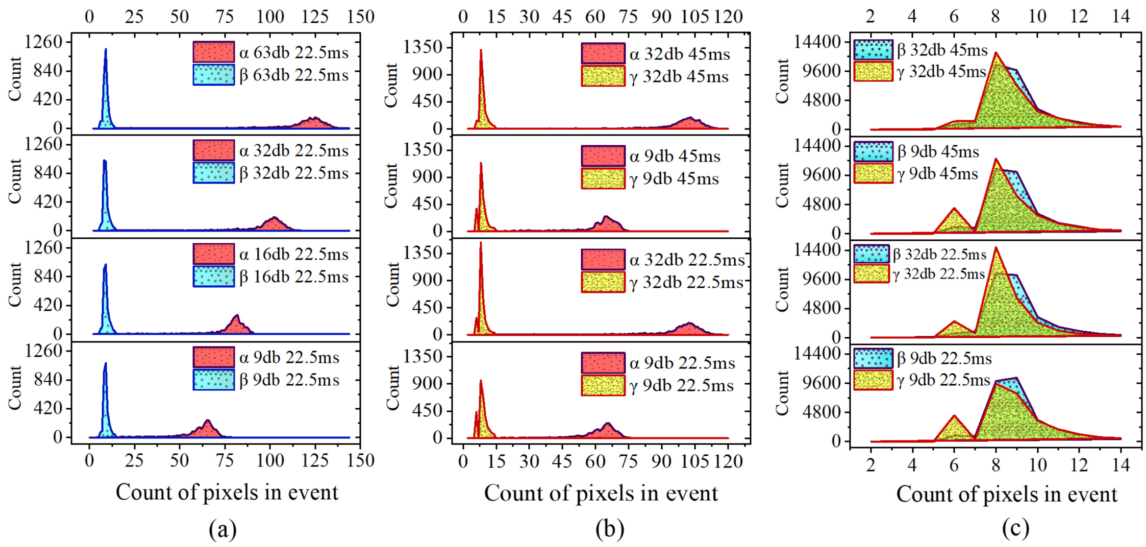


Fig. 17. Comparison of counts of pixels in response events. (a) The number of pixels in the $\alpha$ and $\beta$ response events. (b) The number of pixels in the $\alpha$ and $\gamma$ response events. (c) The number of pixels in the $\beta$ and $\gamma$ response events.

Figure 15 illustrates the relationship between gain, integration time, and the distribution of mean pixel values for response events. From Figures 15(a) and 15(b), it can be observed that as the gain increases, the mean pixel value distribution curves of $\alpha$ and $\beta$ gradually converge. When the gain reaches 63 dB, the curves exhibit significant overlap in the range of mean pixel values from 112 to 135. In contrast, the distribution curves of $\alpha$ and $\gamma$ maintain a certain degree of separation at all gain levels. This indicates that before the gain reaches 32 dB, $\alpha$ events can be effectively identified in the mixed radiation field of the three types by analyzing the differences in mean pixel values. As for $\beta$ and $\gamma$, there is a certain degree of similarity between the two. In Figure 15(c), when the gain is 9 dB, the curves overlap in the range of mean pixel values from 14 to 26. When the gain reaches 32 dB, the overlap range expands to 24 to 70.

Figure 16 illustrates the relationship between gain, integration time, and the distribution of convexity for response events. From Figures 16(a) and 16(b), it can be seen that the convexity of $\alpha$ events is significantly higher than that of $\beta$ and $\gamma$ events. Its curve maintains a certain distance from the $\beta$ and $\gamma$ curves at all gain levels, with a more pronounced separation from the $\gamma$ curve. This suggests that the feature of event convexity can effectively identify $\alpha$ events in the mixed radiation field of the three types. In contrast, the convexity features of $\beta$ and $\gamma$ events exhibit some similarity. In Figure 16(c), the curves corresponding to the two events exhibit significant overlap under all gain conditions, but $\beta$ events are notably more distributed than $\gamma$ events in the region where the convexity exceeds 0.6.

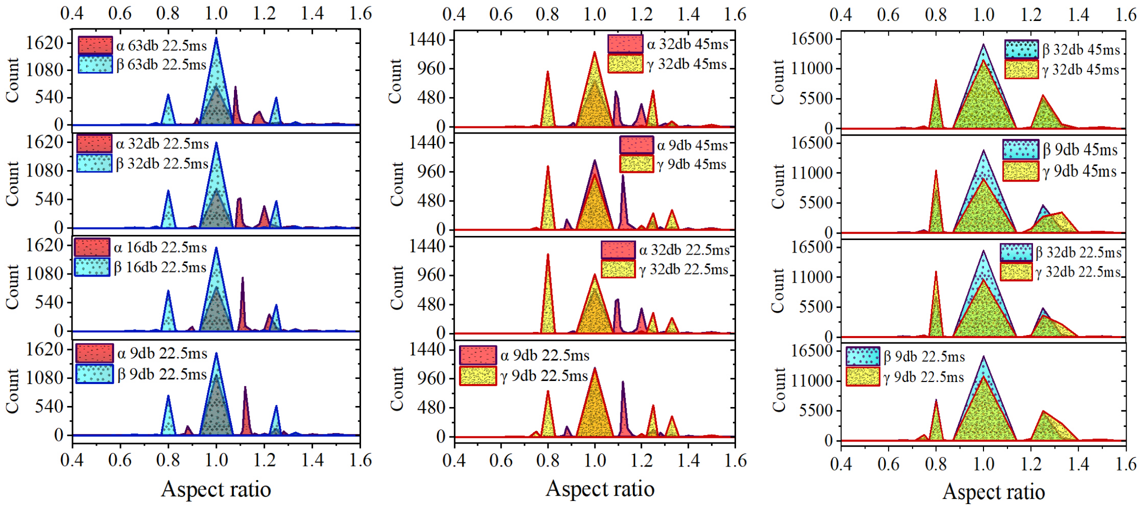


(a) (b) (c)

Fig. 18. Comparison of the aspect ratio of response events: (a) The aspect ratio of $\alpha$ and $\beta$ response events, (b) The aspect ratio of $\alpha$ and $\gamma$ response events, (c) The aspect ratio of $\beta$ and $\gamma$ response events.

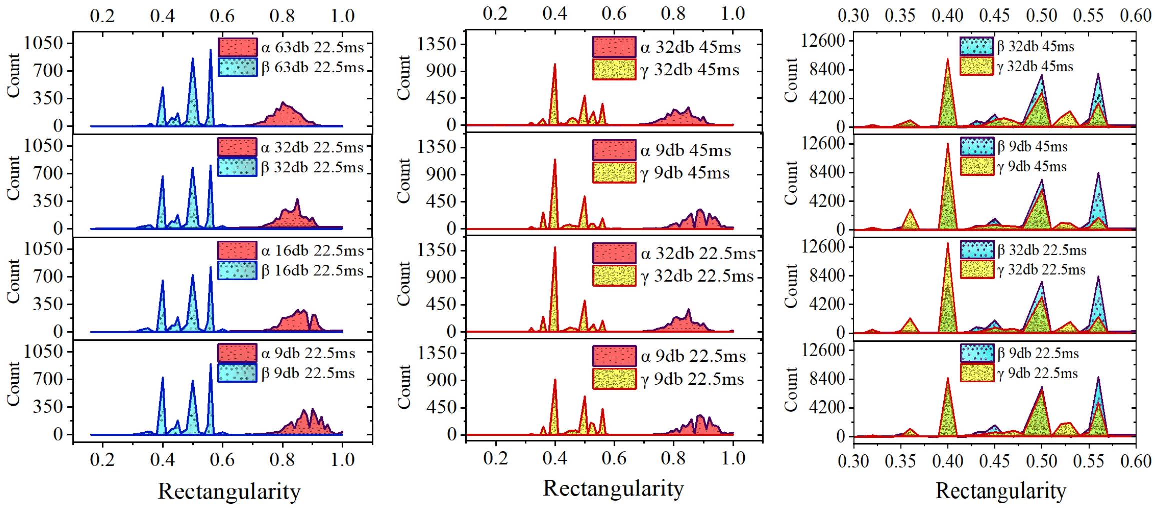


(a) (b) (c)

Fig. 19. Comparison of the rectangularity of response events. (a) The rectangularity of $\alpha$ and $\beta$ response events. (b) The rectangularity of $\alpha$ and $\gamma$ response events. (c) The rectangularity of $\beta$ and $\gamma$ response events.

Figure 17 illustrates the relationship between gain, integration time, and the distribution of the counts of pixels in response events. From Figures 17(a) and 17(b), it can be observed that the counts of pixels in $\alpha$ events are significantly higher than those in $\beta$ and $\gamma$ events. Its curve maintains a certain distance from the $\beta$ and $\gamma$ curves at all gain levels, with a more pronounced separation from the $\gamma$ curve. In contrast, the counts of pixels in $\beta$ and $\gamma$ events do not show significant differences. In Figure 17(c), the distribution curves of the two types of events exhibit significant overlap under all gain conditions, mainly concentrated between 7 and 12 pixels. However, $\gamma$ events are more distributed at 6 pixels than $\beta$ events, and less distributed at 9 pixels than $\beta$ events.

Figure 18 shows the relationship between gain, integration time, and the distribution of the aspect ratio of response events. From Figures 18(a) and 18(b), it can be observed that the distribution peaks of the $\alpha$, $\beta$, and $\gamma$ event curves overlap significantly at an aspect ratio of 1. Additionally, the distribution peak of the $\alpha$ event is closer to 1, and as the gain increases, it gradually shifts towards 1. In contrast, the distribution peaks of the $\beta$ and $\gamma$ events remain relatively stable. After the gain exceeds 32 dB, no significant overlap of the distribution peaks is observed except at the aspect ratio of 1. This indicates that after the gain reaches a certain level, the differences in the aspect ratio of the events can be effectively used to identify the $\alpha$ event in the mixed radiation field of the three events. In contrast, in Figure 18(c), all distribution peaks of the $\beta$ and $\gamma$ events exhibit significant overlap, with some $\gamma$ events distributed in the region where the aspect ratio is greater than 1.3. Although there are some differences be-

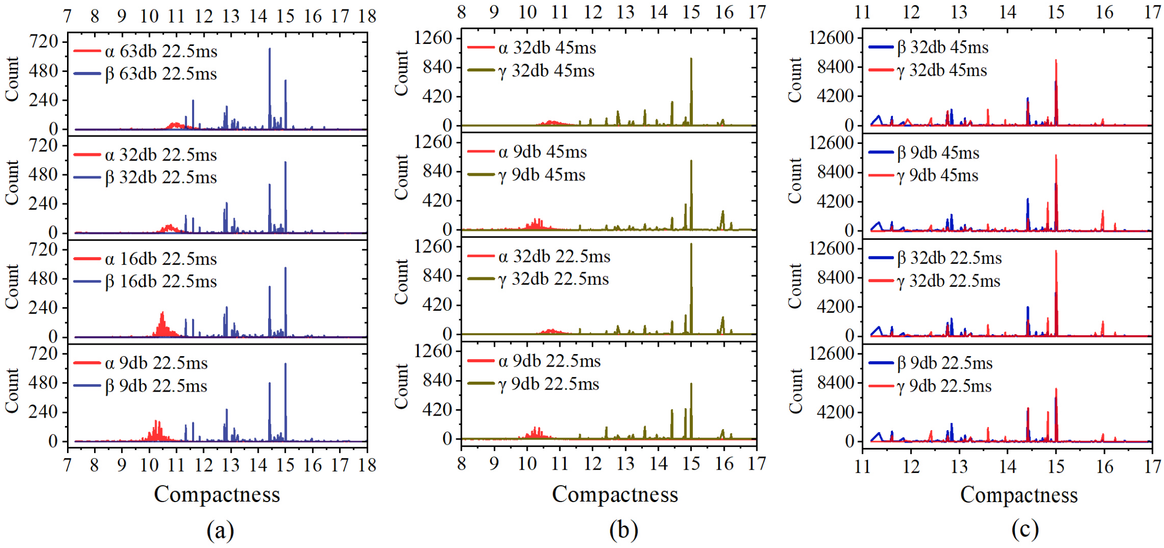


Fig. 20. Comparison of the compactness of response events. (a) The compactness of $\alpha$ and $\beta$ response events. (b) The compactness of $\alpha$ and $\gamma$ response events. (c) The compactness of $\beta$ and $\gamma$ response events.

tween the two events, they do not form a clear distinguishing feature overall, making it very difficult to differentiate the $\beta$ and $\gamma$ events based solely on the aspect ratio distribution.

Figure 19 shows the relationship between gain, integration time, and the distribution of rectangularity of response events. From Figures 19(a) and 19(b), it can be observed that the rectangularity of the $\alpha$ event is significantly higher than that of the $\beta$ and $\gamma$ events. The curve of $\alpha$ remains at a certain distance from the $\beta$ and $\gamma$ curves at all gain levels, with a more pronounced distance from the $\gamma$ curve. This suggests that the features based on event rectangularity can effectively be used to identify the $\alpha$ event in the mixed radiation field of the three events. In contrast, the rectangularity features of the $\beta$ and $\gamma$ events show certain similarities. In Figure 19(c), the curves corresponding to the two events overlap significantly in the regions where the rectangularity is 0.4 and 0.5. Additionally, compared to the $\beta$ event, the $\gamma$ event has a higher distribution near rectangularity values of 0.36 and 0.53, while its distribution at 0.56 is noticeably lower than that of $\beta$.

Figure 20 shows the relationship between gain, integration time, and the distribution of compactness of response events. From Figures 20(a) and 20(b), it can be observed that the compactness of the $\alpha$ event is significantly lower than that of the $\beta$ and $\gamma$ events, and the distribution curve gradually moves closer to that of $\beta$ and $\gamma$ as the gain increases. When the gain exceeds 32 dB, there is a partial overlap with the $\beta$ event in certain regions, but it still maintains a certain distance from the $\gamma$ curve. This indicates that at a certain gain level, the distribution of event compactness can effectively be used to identify the $\alpha$ event in the mixed radiation field of the three events. In contrast, the compactness features of the $\beta$ and $\gamma$ events show certain similarities within a specific range. In Figure 20(c), the curves of the two events have a noticeable intersection in the compactness range of 14 to 15. Furthermore, due to the more flattened shape of the $\gamma$ event compared to $\beta$, some $\gamma$ events have a compactness distribution near 16, while $\beta$ events are distributed around 11.

In summary, at all gain levels, the distributions of average pixel value, pixel count, rectangularity, convexity, and compactness for the $\alpha$ event show significant differences compared to $\beta$ and $\gamma$ events. Therefore, $\alpha$ events can be distinguished in the mixed radiation field based on these features. The features of the $\beta$ and $\gamma$ events are relatively similar. They can be distinguished based on the average pixel value in specific intervals, but there are no significant differences in the distributions of pixel count, rectangularity, convexity, and compactness between the two events. Additionally, the distributions of aspect ratios for the three events are primarily concentrated around 1. Within specific intervals near 1, the distinguishing features are effective for identifying $\alpha$ events.

## V. RESPONSE EVENT TEMPLATE EXTRACTION

Based on the above feature analysis, the response event templates are extracted from dark images. The process primarily includes: binarizing consecutive frame images, identifying and extracting connected regions; analyzing the morphological and structural characteristics of these regions, while also identifying areas with event mixing and edge defects. By verifying the morphology of the connected regions, including the mean pixel value and the counts of pixels contained in the event, events that meet the criteria are selected and their features are labeled. Finally, response events are extracted, and a sample library is constructed. The specific process is shown in Figure 21.

Select dark images with gains of 9 dB and 32 dB. The probability distribution of each pixel value $i$ in the image is $p(i)$, which represents the proportion of pixels with value $i$ relative to the total number of pixels in the image. The weighted pixel mean for each pixel value is calculated as:

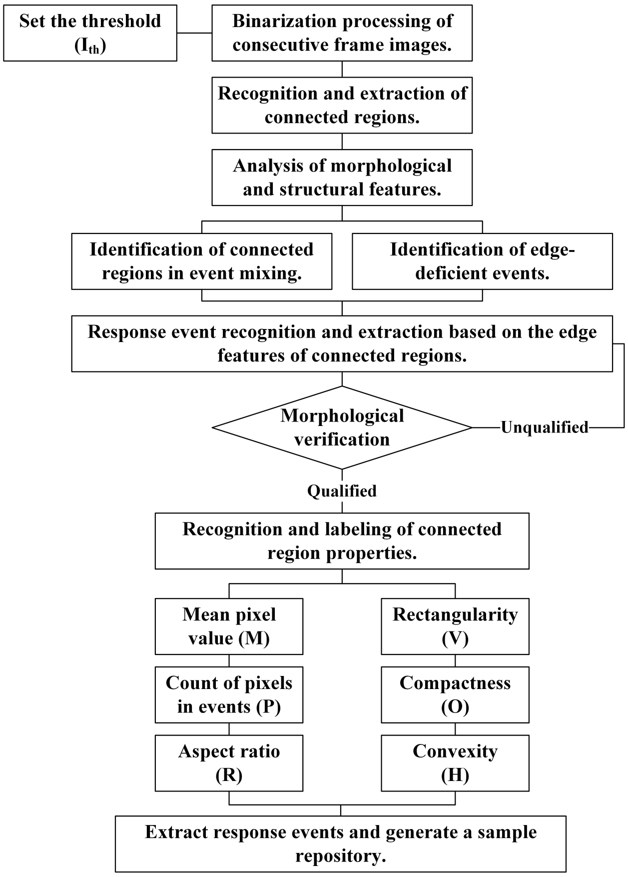


Fig. 21. Template extraction flowchart

$$\mu(i) = i \cdot p(i) \tag{8}$$

Calculate the mean pixel value of the entire image:

$$\mu_g = \sum_{i=0}^{L-1} i \cdot p(i) \tag{9}$$

In the equation, $L$ is the number of pixel values. For any threshold $t$, the pixel values are divided into two classes: foreground (pixel values greater than $t$) and background (pixel values less than or equal to $t$). The weights for these two classes are defined as:

$$\omega_1(t) = \sum_{i=0}^{t} p(i) \tag{10}$$

$$\omega_2(t) = \sum_{i=t+1}^{L-1} p(i) \tag{11}$$

As well as the mean values of the two classes:

$$\mu_1(t) = \frac{1}{\omega_1(t)} \sum_{i=0}^{t} i \cdot p(i) \tag{12}$$

$$\mu_2(t) = \frac{1}{\omega_2(t)} \sum_{i=t+1}^{L-1} i \cdot p(i) \tag{13}$$

The inter-class variance is defined as the variance between different classes or categories:

$$\sigma_b^2(t) = \omega_1(t) \cdot \omega_2(t) \cdot (\mu_1(t) - \mu_2(t))^2 \tag{14}$$

Traverse all possible threshold values $t$, calculate the corresponding inter-class variance, and find the threshold $t$ that maximizes $\sigma_b^2(t)$. The Otsu threshold can be calculated using the following formula:

$$t_{\mathrm{OTSU}} = \arg\max_t \left(\omega_1(t) \cdot \omega_2(t) \cdot (\mu_1(t) - \mu_2(t))^2\right) \tag{15}$$

Let $P$ be the set of pixel points in the image, and $C$ be the set of connected regions. For each pixel point $p \in P$, if $p$ is a foreground pixel, check its neighborhood $N(p)$. If $N(p)$ contains any labeled pixels, label $p$ with the same label as the neighboring pixel. If there are no labeled pixels in $N(p)$, assign a new label to $p$ and add it to $C$.

For each connected region $C_i$, calculate the area $A(C_i)$ and the mean pixel value $M(C_i)$. Based on the distribution range of the number of pixels in $\alpha$ events at 9dB and 32dB, set the minimum threshold $T_1$ and maximum threshold $T_2$; for $\beta$ events, set the minimum threshold $T_3$ and maximum threshold $T_4$ based on the distribution range of the mean pixel value at 9dB and 32dB; for $\gamma$ events, set the minimum threshold $T_5$ and maximum threshold $T_6$ based on the distribution range of the mean pixel value at 9dB and 32dB. The following equation holds:

$$\begin{cases} T_1 \le A(C_i) \le T_2 & \text{Marked as an } \alpha \text{ event} \\ T_3 \le M(C_i) \le T_4 & \text{Marked as a } \beta \text{ event} \\ T_5 \le M(C_i) \le T_6 & \text{Marked as a } \gamma \text{ event} \end{cases} \tag{16}$$

For the labeled event connected regions, calculate the minimum distance $d(C_i)$ from any point on the region's boundary to the image boundary. Set a distance threshold $D$, and the following holds.

$$\begin{cases} d(C_i) \ge D & \text{Retain } C_i \\ d(C_i) < D & \text{Exclude } C_i \end{cases} \tag{17}$$

Label the morphological features of the selected event connected regions, extract the response events, and place them on a solid black background with specified pixel dimensions. The response event templates are divided into three categories: $\alpha$, $\beta$, and $\gamma$ event libraries. The template size for $\alpha$ events is $30 \times 30$, while the template size for $\beta$ and $\gamma$ events is $15 \times 15$. Figure 22 shows the schematic of the response event templates.

## VI. DISCUSSION

We use a CMOS pixel sensor based on morphological features for the identification and extraction of ionizing particles, applying the high-resolution imaging characteristics to radiation detection, thus improving the accuracy and efficiency of ionizing particle identification. Traditional pulse signal discrimination (PSD) techniques typically require a long dead

time, limiting the system's event processing capability, and are prone to misjudgments in the presence of noise interference or pulse pileup. In contrast, CMOS sensors offer faster processing times, enabling rapid responses and effectively overcoming the dead time issue inherent in PSD technology. Furthermore, directly imaging the energy deposition process of ionizing particles within the APS pixel array effectively addresses the noise interference problem. Under low gain conditions, noise in dark images typically manifests as pixel value changes in individual pixels, and the use of the connected region method can easily distinguish noise from response events, thereby improving discrimination accuracy.

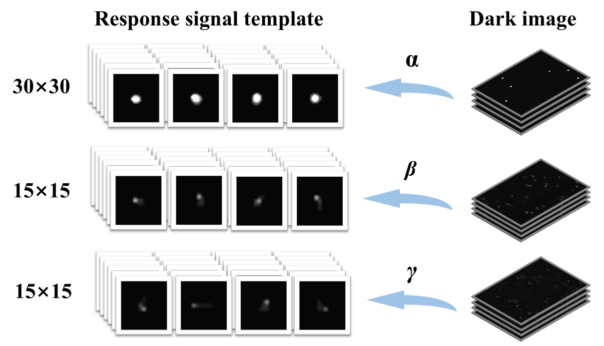


Fig. 22. Typical response event set

Currently, the features of $\alpha$ events are the most distinct and can be identified using a single morphological parameter. However, the features of $\beta$ and $\gamma$ events are quite similar, differing only in average pixel value. Due to the limited morphological features studied, there are still some challenges in the identification process. To address this issue, convolutional neural networks (CNNs) can be used to train templates for response events. The convolutional layers extract local features through local perception, enabling the network to focus on fine details in the image. In dark images, $\beta$ and $\gamma$ events occupy smaller areas and have more varied shapes. By designing specific network structures, more feature information of response events can be extracted to improve differentiation. Therefore, machine learning is a promising approach that can combine more morphological features to enhance the discrimination effectiveness and accuracy of CMOS pixel sensors for response events.

## VII. CONCLUSION

This study presents an innovative approach for ionized particle identification using CMOS imaging and morphological feature analysis. By systematically investigating the spatial morphological characteristics of $\alpha$, $\beta$, and $\gamma$ particle response events, we demonstrated the feasibility of high-resolution particle detection in mixed radiation fields. Key findings include:

(1) Accurate $\alpha$-particle identification: The high spatial resolution of CMOS sensors enables precise localization and identification of $\alpha$-particle response events, leveraging features such as pixel intensity and compactness.

(2) Challenges in $\beta$ and $\gamma$ particle classification: While morphological features like compactness and convexity differentiate $\beta$ and $\gamma$ particles to some extent, significant overlap under high-gain conditions highlights the need for more advanced analysis methods.

(3) Practical implications: This method provides a quantitative foundation for real-time radiation monitoring and classification, addressing critical needs in nuclear safety and environmental monitoring.

Future work will focus on addressing the remaining challenges in particle classification by integrating advanced machine learning algorithms for feature extraction and classification. Additionally, further optimization of CMOS sensors, such as improved noise reduction and sensitivity tuning, will enhance their applicability in complex radiation environments. These developments will expand the practical utility of this approach, paving the way for robust, high-resolution radiation detection technologies.

**Funding** This research is funded by the National Natural Science Foundation of China (11905102).

**Acknowledgements** The authors would like to express their sincere gratitude to the China Institute of Atomic Energy for providing the $^{60}$Co $\gamma$ source and nuclear radiation detector. We acknowledge the support from the Open Fund of the Science and Technology on Reactor System Design Technology Laboratory.

[1] M.D. Alam, S.S. Nasim, and S. Hasan, Recent progress in CdZnTe based room temperature detectors for nuclear radiation monitoring. Prog. Nucl. Energy. **140**, 103918 (2021). https://doi.org/10.1016/j.pnucene.2021.103918

[2] D. Kumar, R. Mesin, and C.S. Chu, Optical fluorescent sensor based on perovskite QDs for nitric oxide gas detection. Appl. Opt. **62**, 486952 (2023). https://doi.org/10.1364/AO.486952

[3] Y. Liu, H. Zhang, and X. Li, Technologies for depth scanning in miniature optical imaging systems Invited. Biomed. Opt. Express. **14**, 507078 (2023). https://doi.org/10.1364/BOE.507078

[4] F. Madonini, F. Severini, F. Zappa et al., Single Photon Avalanche Diode Arrays for Quantum Imaging and Microscopy. Adv. Quantum Technol. **27**, 2100005 (2021). https://doi.org/10.1002/qute.202100005

[5] J.J. Ma, D.X. Zhang, D. Robledo et al., Ultra-high-resolution quanta image sensor with reliable photon-number-resolving and high dynamic range capabilities. Sci. Rep. **12**, 13869 (2022). https://doi.org/10.1038/s41598-022-17952-z

[6] R.H. Hadfield, J. Leach, F. Fleming et al., Single-photon detection for long-range imaging and sensing. Optica. **10**, 488853 (2023). https://doi.org/10.1364/OPTICA.488853

[7] N.A.W. Dutton, I. Gyongy, L. Parmesan et al., A SPAD-Based QVGA Image Sensor for Single-Photon Counting and Quanta Imaging. IEEE Trans. Electron Devices. **63**, 2464682 (2016). https://doi.org/10.1109/TED.2015.2464682

[8] R. He, X.Y. Niu, Y. Wang et al., Advances in nuclear detection

and readout techniques. Nucl. Sci. Tech. **34**, 205 (2023). https://doi.org/10.1007/s41365-023-01359-0

[9] A. Chakraborty, N. Parashar, D.K. Pandey et al., Radiological complexity of nuclear facilities: an information complexity approach to workplace monitoring. J. Radiol. Prot. **44**, 021511 (2024). https://doi.org/10.1088/1361-6498/ad42a5

[10] R. Scott, W. Jiang, and M.J. Deen, CMOS Time-to-Digital Converters for Biomedical Imaging Applications. IEEE Rev. Biomed.Eng. **16**, 3092197 (2023). https://doi.org/10.1109/RBME.2021.3092197

[11] P. Yepiz-Graciano, Z. Ibarra-Borja, R.R. Alarcón et al., Quantum Optical Coherence Microscopy for Bioimaging Applications. Phys. Rev. Applied. **18**, 034060 (2022). https://doi.org/10.1103/PhysRevApplied.18.034060

[12] M. Gersbach, Y. Maruyama, R. Trimananda et al., A Time-Resolved, Low-Noise Single-Photon Image Sensor Fabricated in Deep-Submicron CMOS Technology. IEEE J. Solid-State Circuits. **47**, 2188466 (2012). https://doi.org/10.1109/JSSC.2012.2188466

[13] L.L. Li, S. Kumar, Y.M. Sua, and Y.P. Huang, Noise-resilient single-pixel compressive sensing with single photon counting. Commun. Phys. **7**, 110 (2024). https://doi.org/10.1038/s42005-024-01603-y

[14] T. Polakovic, W. Armstrong, G. Karapetrov et al., Unconventional Applications of Superconducting Nanowire Single Photon Detectors. Nanomaterials. **10**, 1198 (2020). https://doi.org/10.3390/nano10061198

[15] L.X. You, Superconducting nanowire single-photon detectors for quantum information. Nanophotonics. **9**, 0186 (2020). https://doi.org/10.1515/nanoph-2020-0186

[16] G.V. Resta, L. Stasi, M. Perrenoud et al., Gigahertz Detection Rates and Dynamic Photon-Number Resolution with Superconducting Nanowire Arrays. Nano Lett. **23**, 3c01228 (2023). https://doi.org/10.1021/acs.nanolett.3c01228

[17] D.H. Pan, J. Sheng, X.Y. Wang et al., In vivo SPECT imaging of an $^{131}$I-labeled PM 2.5 mimic substitute. Nucl. Sci. Tech. **31**, 111 (2020). https://doi.org/10.1007/s41365-020-00818-2

[18] P. Huang, S.Q. Li, R.D. Yang et al., Photon energy response optimization using few-channel spectroscopy dose method for Si-PIN photodetector applied in personal dose equivalent measurements. Nucl. Sci. Tech. **31**, 36 (2020). https://doi.org/10.1007/s41365-020-0748-2

[19] X.D. Guo, P.He, X.J. Lv et al., Material decomposition of spectral CT images via attention-based global convolutional generative adversarial network. Nucl. Sci. Tech. **34**, 45 (2023). https://doi.org/10.1007/s41365-023-01184-5

[20] J.Z. Yang, M.F. Li, X.X. Chen et al., Single-photon quantum imaging via single-photon illumination. Appl. Phys. Lett. **117**, 214001 (2020). https://doi.org/10.1063/5.0021214

[21] Q.Q. Cheng, C.W. Ma, Y.Z. Yuan et al., X-ray detection based on complementary metal-oxide-semiconductor sensors. Nucl. Sci. Tech. **30**, 9 (2019). https://doi.org/10.1007/s41365-018-0528-4

[22] D. Krüger, A.Y. Zhang, B. Aghelnejad et al., A Portable CMOS-Based Spin Resonance System for High-Resolution Spectroscopy and Imaging. IEEE J. Solid-State Circuits. **58**, 3274043 (2023). https://doi.org/10.1109/JSSC.2023.3274043

[23] M. Esposito, T. Price, T. Anaxagoras et al., Geant4-based simulations of charge collection in CMOS Active Pixel Sensors. J. Instrum. **12**, P03028 (2017). https://doi.org/10.1088/1748-0221/12/03/P03028

[24] J. Florczak, T. Neubert, K. El Maghawry et al., Radiation Monitor Extension for CMOS Imaging Instruments in Nanosatellites. IEEE Trans. Nucl. Sci. **69**, 3144784 (2022). https://doi.org/10.1109/TNS.2022.3144784

[25] F. Lin, R.M. Xie, H.Y. Li et al., Counting alpha particles produced by radon daughters using commercial off-the-shelf complementary metal oxide semiconductor (COTS CMOS) image sensors. J. Instrum. **19**, T04001 (2024). https://doi.org/10.1088/1748-0221/19/04/T04001

[26] H. Mahmoudi, S.S.K. Poushi, B. Steindl et al., Optical and Electrical Characterization and Modeling of Photon Detection Probability in CMOS Single-Photon Avalanche Diodes. IEEE Sens. J. **21**, 3051365 (2021). https://doi.org/10.1109/JSEN.2021.3051365

[27] Y.M. Aneesh and B. Bindu, Comparative Analysis of Single Event Transients in InGaAs-OI/Bulk/BOI FinFETs for SET-Tolerant InGaAs/Ge-OI Complementary FinFET Circuits. IETE J. Res. **70**, 2204836 (2024). https://doi.org/10.1080/03772063.2023.2204836

[28] P.M. Johns and J.C. Nino, Room temperature semiconductor detectors for nuclear security. J. Appl. Phys. **126**, 040902 (2019). https://doi.org/10.1063/1.5091805

[29] W.Z. Li, J.X. Cheng, F. Liu et al., Research on the Technological Progress of CZT Array Detectors. Sensors. **24**, 725 (2024). https://doi.org/10.3390/s24030725

[30] H.Q. Huang, X.F. Yang, W.C. Ding et al., Estimation method for parameters of overlapping nuclear pulse signal. Nucl. Sci. Tech. **28**, 12 (2017). https://doi.org/10.1007/s41365-016-0161-z

[31] H.Q. Zhang, H.T. Shi, Z.D. Li et al., Digitalization of inverting filter shaping circuit for nuclear pulse signals. Nucl. Sci. Tech. **31**, 86 (2020). https://doi.org/10.1007/s41365-020-00799-2

[32] Z.K. Fan, J.L. Sun, H.X. Li et al., A novel method for simultaneous measurement of $^{222}$Rn and $^{220}$Rn progeny concentrations measured by an alpha spectrometer. Nucl. Sci. Tech. **36**, 8 (2025). https://doi.org/10.1007/s41365-024-01570-7

[33] C. Zhao, W. Jin, Y. Shi et al., Utilizing BP neural networks to accurately reconstruct the tritium depth profile in materials for BIXS. Nucl. Sci. Tech. **36**, 15 (2025). https://doi.org/10.1007/s41365-024-01569-0

[34] G. Giacalone, Beyond axial symmetry: high-energy collisions unveil the ground-state shape of $^{238}$U. Nucl. Sci. Tech. **35**, 218 (2024). https://doi.org/10.1007/s41365-024-01582-3